

SPECIAL: Single-Shot Projection Error Correction Integrated Adversarial Learning for Limited-Angle CT

Dianlin Hu^{ID}, Yikun Zhang^{ID}, Jin Liu^{ID}, Changping Du, Jinglin Zhang, Shouhua Luo, Guotao Quan^{ID}, Qiegen Liu^{ID}, Senior Member, IEEE, Yang Chen^{ID}, Senior Member, IEEE, and Limin Luo, Senior Member, IEEE

Abstract—Limited-angle CT is an indispensable tool for some practical applications when the projection data can be only collected within a limited-angle range due to the constraints of scanning conditions. However, the limited-angle scanning mode will lead to severely degraded images with excessive artifacts. Meanwhile, existing methods fail to reconstruct satisfactory images in limited-angle CT because of the unguaranteed measurement consistency caused by serious projection missing. In this paper, we developed a method termed Single-shot Projection Error Correction Integrated Adversarial Learning (SPECIAL) progressive-improvement strategy, which could effectively combine the complementary information contained in the image domain and projection domain, and greatly improve the reconstructions at the expense of small computational cost. Specifically, enhanced adversarial learning is used in different stages to remove artifacts without losing high-frequency component. A projection error correction module is used to boost the performance in high-attenuation tissue restoration. Compared with other competitive algorithms, quantitative and

Manuscript received December 7, 2020; revised April 27, 2021 and June 28, 2021; accepted July 12, 2021. Date of publication July 26, 2021; date of current version August 4, 2021. This work was supported in part by the State's Key Project of Research and Development Plan under Grants 2017YFC0109202 and 2017YFA0104302, in part by the National Natural Science Foundation under Grant 61871117, in part by the Science and Technology Program of Guangdong under Grant 2018B030333001. (*Corresponding authors:* Qiegen Liu; Yang Chen.)

Dianlin Hu, Yikun Zhang, Changping Du, and Limin Luo are with the Laboratory of Image Science and Technology, Southeast University, Nanjing 210096, China and with the Centre de Recherche en Information Biomédicale Sino-Français (LIA CRIBs), Rennes F-3500, France, and also with the Key Laboratory of Computer Network and Information Integration (Southeast University), Ministry of Education, Nanjing 210096, China (e-mail: dianlin@seu.edu.cn; yikun@seu.edu.cn; 220191716@seu.edu.cn; luo.list@seu.edu.cn).

Jin Liu is with the College of Computer and Information, Anhui Polytechnic University, Wuhu 241000, China (e-mail: liujin@ahpu.edu.cn).

Jinglin Zhang is with the School of Artificial Intelligence, Hebei University of Technology, Tianjin 300131, China (e-mail: jinglin.zhang37@gmail.com).

Shouhua Luo is with the Department of Biomedical Engineering, Southeast University, Nanjing 210096, China (e-mail: luoshouhua@seu.edu.cn).

Guotao Quan is with the CT RPA Department, United Imaging Healthcare Co., Ltd., Shanghai 201807, China (e-mail: guotao.quan@united-imaging.com).

Qiegen Liu is with the Department of Electronic Information Engineering, Nanchang University, Nanchang 330031, China (e-mail: liuqiegen@ncu.edu.cn).

Yang Chen is with the Laboratory of Image Science and Technology, Southeast University, Nanjing 210096, China and with the School of Cyber Science and Engineering, Southeast University, Nanjing 210096, China, and also with the Key Laboratory of Computer Network and Information Integration (Southeast University), Ministry of Education, Nanjing 210096, China (e-mail: chenyang.list@seu.edu.cn).

This article has supplementary downloadable material available at <https://doi.org/10.1109/TCI.2021.3098922>, provided by the authors.

Digital Object Identifier 10.1109/TCI.2021.3098922

qualitative results show that the proposed method could make a promising improvement on artifact removal, edge preservation and tiny structure restoration.

Index Terms—Limited-angle CT reconstruction, measurement consistency, enhanced adversarial learning, high-frequency constraint, projection correction.

I. INTRODUCTION

X-RAY Computed Tomography (CT) has been widely used in medical diagnosis, industrial detection and security check [1] since it was invented. However, in some CT practices [2], [3], the projection data are only collected from a limited-angle range because of the limitation of scanning conditions. Under these circumstances, incomplete projection data could lead to severe artifacts in reconstructed images, which significantly compromises the diagnostic value. Different from other inverse problems in CT imaging, the challenge in limited-angle CT is that the measured data is collected only in a limited angular range, which means the projection data is incomplete. Therefore, limited-angle CT reconstructions suffer from vast divergence phenomenon in object edges. To tackle this challenge, numerous algorithms have been developed for limited-angle CT reconstruction. These can be categorized into the following categories: analytical methods, iterative methods and deep-learning (DL)-based methods.

Filtered Back Projection (FBP) is a typical analytic method, which is efficient and widely employed. Nevertheless, it heavily relies on the complete projection data. FBP algorithm fails to reconstruct high-quality images and leads to shadow artifacts when lacking most measurements. Meanwhile, to make full use of the available projection data, numerous iterative reconstruction (IR) algorithms have been proposed for limited-angle CT reconstruction. Simultaneous algebraic reconstruction technique (SART) is a classical IR approach and performs more competitively in noise reduction and artifact removal compared with FDK when the projection data is incomplete. However, it still encounters obvious artifacts when the scanning angle is insufficient [4]. Later, total variation (TV) constraint was utilized with the assumption that the gradients of CT images were sparse and it outperformed SART in limited-angle CT reconstruction [5]. Further, Chen *et al.* proposed an anisotropic TV (ATV) minimization method to improve the FBP reconstructed images [6]. To overcome the

weakness of TV in removing metal artifacts when the projection was incomplete, Wang *et al.* regularized the wavelet coefficients and achieved superior performance in preserving the edges of images and suppressing the metal artifacts [7]. L_0 -norm is another commonly used prior knowledge for limited-angle CT reconstruction, which can provide a more sparse solution compared with TV [8], [9]. Yu *et al.* investigated the influence of L_0 -norm image gradient prior on limited-angle CT reconstruction and demonstrated its advantages in edge restoration and artifact reduction [10]. To reduce the tendency of over smoothing in TV, Sun *et al.* introduced the L_0 -norm discrete gradient transform to improve the reconstruction quality [11]. Besides, low rank [12], wavelet transform [13] and sparse representation [14] are also the popular priors for regularized reconstructions. Nevertheless, these methods have some defects, including high computational cost and sensitive hyper-parameter selection. At the same moment, IR methods could obtain high-quality images when dealing with light artifacts, but the performance is often lowered when IR methods attempt to remove severe artifacts [15].

Recently, DL-based methods have attracted rapidly increasing attention in many medical imaging tasks [16]–[18]. Specifically, convolutional neural network (CNN) based methods have been developed for CT reconstruction and achieved impressive performance over traditional algorithms [19]–[22]. To make full use of the comprehensive domain information, Zhang *et al.* implemented an end-to-end framework (hdNet) to suppress streak artifacts in limited-angle CT reconstruction [23]. Aided by the complementary information contained in the sinogram domain and image domain, hdNet can significantly improve the reconstruction. With the limitation of computational resources, it is difficult for deep learning to map projection data into reconstructed images directly. Therefore, Würfl *et al.* designed a new back-projection layer to reconstruct images from cone-beam limited-angle projection data and gained an obvious improvement over analytical methods [24]. Nevertheless, the mentioned algorithms tend to blur reconstructed images because they only utilize the L_1 - or L_2 -minimization. Fortunately, the generative adversarial network (GAN) is an effective technique against low contrast and smoothness by reducing the distribution distances, which has gained numerous applications in the field of image restoration [25]–[27]. To obtain the missing projection data closing to the real measurements, Anirudh *et al.* proposed a novel CT-Net to predict the invisible sinogram data with the combination of 1D CNN and GAN [28], and the experimental results indicated that CT-Net outperformed existing solutions in 3D structure preservation. Later, Liu *et al.* proposed a reconstruction method termed TomoGAN [29] for sparse-view CT and low-dose CT, which combined the WGAN [27] and perceptual loss to improve the reconstruction images. Experiments showed that TomoGAN outperformed conventional algorithms. Unfortunately, these CNN- and GAN-based reconstruction methods cannot provide measurement consistency which cannot provide the guarantee on the worst performance for the reconstructed image [30]. Model-based methods are usually reliable because they are able to ensure measurement consistency. Measurement consistency defines the distance between the reprojection data of reconstructed images and available projection data, which

is necessary for final images to prevent fake structures. Being aware of the significance of measurement consistency, Bubba *et al.* fused IR framework with deep learning to infer the invisible parts, which could decrease the task difficulty for deep learning [31]. Consequently, extensive experiments showed that [31] surpassed both model-based methods and data-based methods. Moreover, due to the fact that deep learning is able to provide more powerful regularized effects compared with hand-crafted priors, therefore, data-driven methods can be integrated into the model-based framework by replacing the traditional prior constraint. Wang *et al.* combined the alternating direction method of multipliers and deep learning (ADMMDR) for limited-angle CT reconstruction [32]. The experimental results showed that ADMMDR was good at structure preservation and artifact reduction.

Accordingly, this paper proposes a Single-shot Projection Error Correction Integrated Adversarial Learning (SPECIAL) framework for limited-angle CT reconstruction. SPECIAL adopts a progressive-improvement (PI) strategy, which can gradually improve the reconstructed images. First, we employ the enhanced adversarial learning to remove shadow artifacts. To preserve the sharp edges and avoid smoothing structures, high-frequency components of reconstructed images are additionally assessed in the discriminative process. However, the reconstructed results in the previous phase have inaccurate CT numbers in high-attenuation regions. Therefore, inspired by the IR methods, the reconstructed images are updated via the data consistency constraint to correct these errors. The same adversarial learning is applied again to compensate for the artifacts brought by the FDK operator. These stages are independent, which means every step can be trained or processed offline and not strictly limited by computational resources. The main contributions of this paper are in the following four aspects: First, the high-frequency component in CT images is underlined by adversarial learning to enhance the performance of SPECIAL in edge preservation. Second, a lightweight corrected operator is implemented to ensure measurement consistency. Third, the SPECIAL framework can be applied to cone-beam CT in practical applications since SPECIAL is an offline iterative reconstruction method. Most advanced reconstruction algorithms [33], [34] involve several projection and backprojection operations online, which need high computational resources. Therefore, it is hard for them to be applied in cone-beam CT imaging. Fourth, the proposed method is a flexible plug-and-play tool, which can be easily extended for other imaging tasks. Experimental results show that SPECIAL can lead to superior performance in edge preservation, artifact suppression and tissue restoration.

The rest of this article is organized as follows. Section II introduces the details of SPECIAL framework. In Section III, simulated and real data results are performed and the mechanism of the proposed method will be analyzed. In Section IV, we will discuss some related issues and make a plan for future work.

II. METHODOLOGY

A. Dense Encoder-Decoder Network

Generator is the essential component in GAN model, and we apply a Dense Encoder-Decoder Network (DEDN) as the

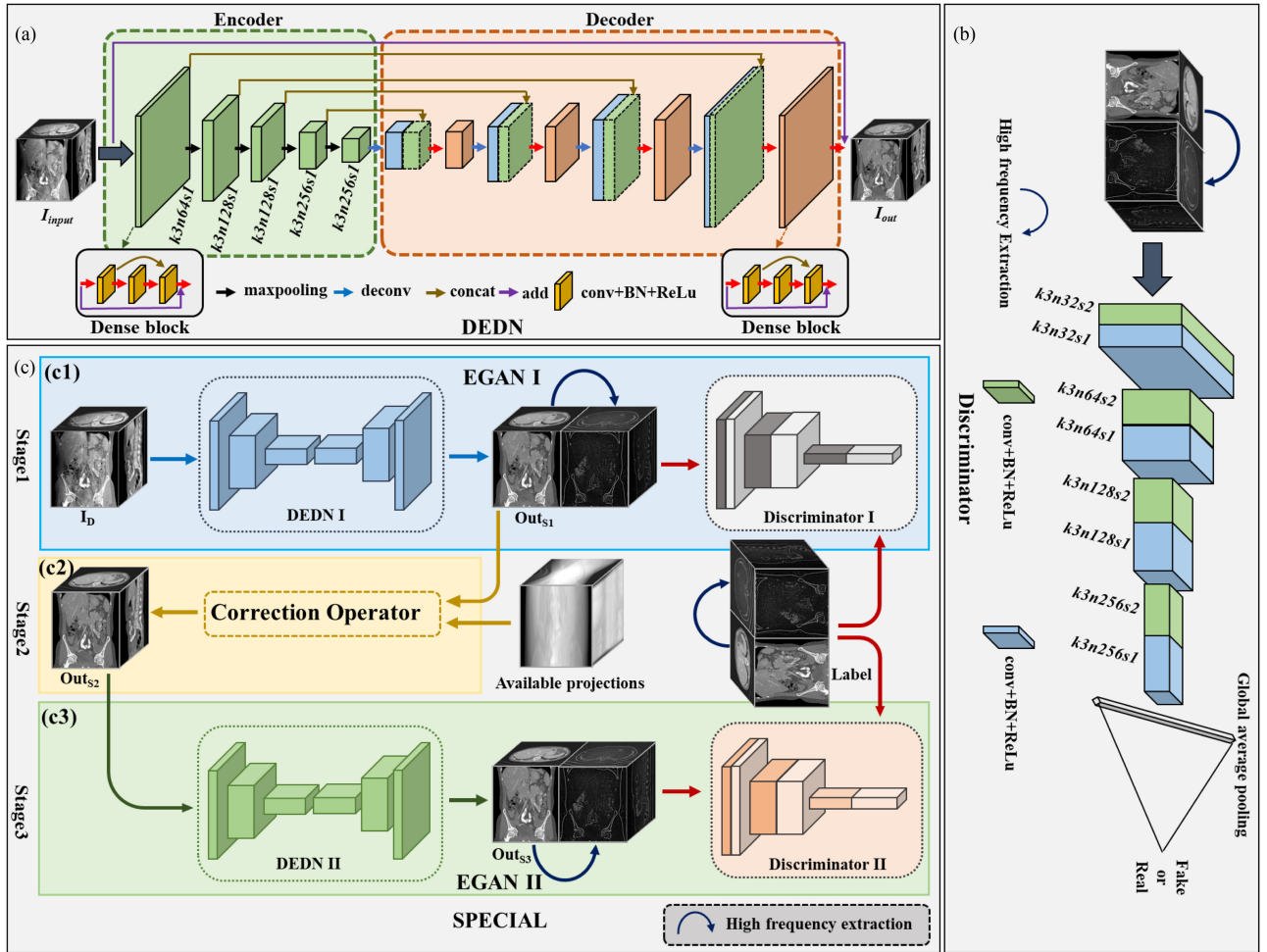


Fig. 1. The architecture of our proposed method. (a) is the structure of DEDN, (b) is the structure of the discriminator, (c) is the overview of the SPECIAL framework. All the labels used in the SPECIAL framework are reconstructed by the FDK method from the full-view noise-free projection data.

generator. From Fig. 1(a), we can notice that DEDN consists of two modules: encoder and decoder. Encoder aims to extract essential features lied on the low-dimensional manifold by gradually shrinking feature maps with max-pooling operators. Because the low-dimensional manifold has the robustness to perturbation and noise [35], the decoder is able to effectively recover satisfactory results from the encoding space by gradually enlarging feature maps with deconvolutional layers (implemented by the transpose convolutions). Additionally, skip connections are also necessary elements in encoder-decoder-based structures [36]–[38]. Such skip connections concatenate low-level and fine-grained features with high-level and abstract features together, which can avoid detail missing and accelerate the information flow [21].

1) *Residual Dense Block*: Residual dense block (RDB) is the basic element of DEDN demonstrated in Fig. 1(a). RDB adopts a local residual learning strategy to avoid vanishing or exploding gradients [21]. It has been widely used in the field of image processing [39]–[41]. Residual learning can promote the information flow by combining input features and output features together, which accelerates the back-propagation of gradients and speeds up the convergence and reduces the training difficulty

[40]. Further, to take full advantage of low-level features, densely connected layers are also employed in our RDB [42]. Dense blocks concatenate their previous layers as the input vector for subsequent layers, which contributes to feature map reuse and parameter reduction compared with residual learning [43], [44]. Besides the residual learning and dense connection, BN [45] and ReLu [46] are also employed to accelerate the network training and improve the network capacity.

B. High-Frequency Enhancement Module

CNN-based methods have better performance in handling low-frequency features than high-frequency features [23], [28], [31], [32]. Here, we utilize an enhanced generative adversarial learning network (EGAN) to boost edge preservation [47]. In this EGAN model, the generated images are integrated with high-frequency component before put into the discriminator to guide the DEDN to produce more realistic results. High-frequency component extraction in Fig. 1(b) can be described as:

$$H_I = I - F(I, g) \quad (1)$$

where $g \sim N(\mu, \sigma^2)$ is the filtering kernel and F is the filtering operation. The image I is blurred first to acquire the low-frequency component, which is then subtracted from the original image to provide the high-frequency component H_I . By additionally constraining the high-frequency component, EGAN will guide the generator to produce results with higher contrast. The cost function for EGAN is defined as follows:

$$\begin{aligned} \min_{G} \max_{D} L_{EGAN}(D, G) = & -E_x[D(C(I_{ND}, H_{ND}))] \\ & + E_z[D(C(G(I_D), H_{G(I_D)}))] \\ & + \lambda \cdot E_{\hat{x}}[(\nabla_{\hat{x}}(D(\hat{x}))_2 - 1)^2] \end{aligned} \quad (2)$$

where D is the discriminator and G denotes the generator. C is the concatenation operator, I_{ND} is the reference image reconstructed by FDK algorithm from full-view noise-free projection and I_D is the degraded image reconstructed by FDK method from limited-angle porjections. H_{ND} and H_D are the high-frequency components of I_{ND} and I_D , respectively. $\hat{x} = \alpha \cdot C(I_{ND}, H_{ND}) + (1 - \alpha) \cdot C(G(I_D), H_{G(I_D)})$ is uniformly sampled along straight lines connecting pairs of $C(I_{ND}, H_{ND})$ and $C(G(I_D), H_{G(I_D)})$. Moreover, to obtain stable training, we adopt Wasserstein GAN [27] with gradient penalty to optimize the discriminator parameters. More parameter settings can be found in the *experimental section*. Both EGAN and TomoGAN are WGAN-based methods, but there are significantly different as follows. (a) The DEDN adopts residual dense block based on the U-shape structure for the improvement of feature extraction. (b) EGAN additionally evaluates the high-frequency components of generated images.

C. Single-Shot Projection Error Correction

Measurement consistency provides reliable insurance on the worst-case performance [30]. In traditional IR methods, the data fidelity term is used to guarantee this consistency but at the cost of higher computational requirement [48]. In order to reduce the running time without compromising the quality of reconstructed results, Shi *et al.* proposed a novel iterative strategy, where the back-projection was replaced by FBP operator to accelerate convergence [49]. Inspired by this, to exploiting knowledge based on measurement consistency, the FDK algorithm is adopted to reconstruct error images as a correction operator. This procedure can be expressed as follows, which is matched with Fig. 1(c2):

$$I_{error} = FDK(Y - POut_{s1}) \quad (3)$$

$$Out_{s2} = Out_{s1} + max(I_{error}, 0) \quad (4)$$

where Y is the collected projection data, and Out_{s1} denotes the images reconstructed from the first stage of SPECIAL framework (more information about Out_{s1} can be found in the next section). In Eq. (3), we first calculate the projection error between the reprojeciton of reconstructed images Out_{s1} (via the system matrix P) and referred limited-angle projection data Y . Then, the FDK operator is used to reconstruct the corrected maps I_{error} which approximate the differences between Out_{s1} and real images. Moreover, in Eq. (4), to particularly improve the performance of Out_{s1} in high-attenuation regions, we employ

a positive constraint on I_{error} . Consequently, we can obtain the corrected images Out_{s2} with more tissue details than Out_{s1} .

D. SPECIAL Framework

In this work, we formulate the total optimization problem as:

$$\theta^* = \operatorname{argmin}_{\theta} L(f_{\theta}(I_D), I_{ND}) \quad (5)$$

where f_{θ} is the optimized network with parameter θ to generate high-quality CT results from I_D , and L is the metric function to measure the similarity between $f_{\theta}(I_D)$ and I_{ND} . To address Eq. (5), SPECIAL employs a PI strategy, which consists of three stages illustrated in Fig. 1(c1)-(c3). Notice that the three phases are independent of each other rather than an end-to-end optimization process.

In the first stage of SPECIAL, the minimized objective function is Eq. (6), which corresponds to the Fig. 1(c1):

$$\begin{aligned} \min_{G_I} \max_{D_I} L_{MSE}(G_I(I_D), I_{ND}) \\ + \lambda_1 \cdot L_{SSIM}(G_I(I_D), I_{ND}) \\ + \beta_1 \cdot L_{EGAN}(D_I, G_I) \end{aligned} \quad (6)$$

where the pixel-wise cost functions L_{MSE} and L_{SSIM} are used to optimize the generator. Besides, the enhanced adversarial loss L_{EGAN} is also applied via EGAN I to preserve edges. Specifically, we utilize DEDN I as the generator G_I and the network depicted in Fig. 1(b) as the discriminator D_I . DEDN I takes the degraded images I_D reconstructed by FDK algorithm from the limited-angle projection data as the input to produce reconstructed images Out_{s1} via $G_I(I_D)$. In order to promote the performance of DEDN I in terms of edges, Out_{s1} integrated with its high-frequency component is additionally supervised by EGAN I to enhance edge preservation.

However, Out_{s1} performs worse in some regions with large attenuation coefficients. Therefore, we propose a single-shot projection error correction (shown in Fig. 1(c2)) to alleviate this issue. With the FDK operator, the error maps are efficiently transformed from the sinogram domain into the image domain with a lowered computational cost. This procedure leads to improved reconstruction Out_{s2} (more information can be found in Eqs. (3)-(4)) by incorporating measurement consistency derived from available projection data.

It is also observed that such single-shot error correction tends to bring secondary artifacts caused by FDK. To tackle this issue, we adopt the following optimization procedure in the third stage of the SPECIAL framework as observed in Fig. 1(c3):

$$\begin{aligned} \min_{G_{II}} \max_{D_{II}} L_{MSE}(G_{II}(Out_{s2}), I_{ND}) + \lambda_2 \\ \cdot L_{SSIM}(G_{II}(Out_{s2}), I_{ND}) + \beta_2 \cdot L_{EGAN}(D_{II}, G_{II}) \end{aligned} \quad (7)$$

Similar to Eq. (6), a refined result $Out_{s3} = G_{II}(Out_{s2})$ can be obtained via this procedure. All the hyper-parameter settings in Eq. (6) and Eq. (7) can be found in the *experimental section*.

Although the networks in different stages have the same architectures, they are actually different and trained twice for

Algorithm I: SPECIAL.

Training Phase

Input: $Y, I_{ND}, I_D, \lambda_1, \lambda_2, \beta_1, \beta_2$.

Stage 1: Optimize the Eq. (6) to get the trained network G_I, D_I and the results Out_{S1} via $G_I(I_D)$.

Stage 2: Obtain the results Out_{S2} via Eqs. (3)-(4).

Stage 3: Minimize the Eq. (7) to get the trained network G_{II} and D_{II} .

Return: Trained networks G_I, G_{II} .

Testing Phase

Input: Y, I_D, G_I, G_{II} .

Stage 1: Generate Out_{S1} via $G_I(I_D)$.

Stage 2: Obtain Out_{S2} via Eqs. (3)-(4).

Stage 3: Get Out_{S3} via $G_{II}(Out_{S2})$.

Return: Final results Out_{S3} .

various purposes. The DEDN used in the first stage aims to remove severe artifacts and restore tissue details, and the target of the DEDN in the last step is to refine the results provided by the previous phase. The workflow of SPECIAL framework is summarized in Algorithm I.

III. RESULTS

All the DL-based methods are implemented in Tensorflow framework with Python language and the traditional reconstruction approaches are performed in MATLAB 2018a on a PC (CPU is Inter(R) Xeon(R) E5-2683, 2 GHZ, GPU is NVIDIA GTX1080Ti with 11G memory, RAM is 64GB). The hyper-parameter settings and training details for SPECIAL are configured as follows. Guided by the extensive experiments, λ_1 and λ_2 are set to 10000, β_1 and β_2 are 0.05, respectively. λ is set to 10 according to [47]. All the EGANs are optimized by Adam algorithm [50]. The learning rate is slowly decreased from 10^{-3} to 10^{-5} . To validate the effectiveness of the proposed SPECIAL framework, the FDK algorithm (Ramp-filter), total variation (TV), DDNet [44], MSWDNet [51], DCAR algorithm [52] are treated as comparisons. Meanwhile, the root mean square error (RMSE), peak single-to-noise ratio (PSNR) and structure similarity index (SSIM) [53] are applied to evaluate the reconstruction results of various methods quantitatively. All the DL-based methods are trained individually for each reconstruction to obtain high-quality CT images.

A. Simulated Data Results

The CT data used in simulated experiments were provided by the AAPM Low Dose CT Grand Challenge. From the total ten patients, we selected eight patients for training and the rest patients for testing. In this study, we adopted cone-beam scanning mode to generate training samples where the distance from the source to object and detector were 50 cm and 100 cm, respectively. The detector had 900×400 elements, and each of them covered an area of 1.5×1.5 mm 2 . 960 projections were collected via 360° as full-sampled projection data. The photon number of each X-ray path is 10^6 , which represents

the normal dose level [54]. The reconstructed volumes have the size of $512 \times 512 \times 200$, and every pixel covered an area of $0.9 \times 0.9 \times 0.9$ mm 3 . The reference images were reconstructed by the FDK algorithm via full-sampled projection data. To validate the performance of the SPECIAL framework, limited-angle CT images reconstructed from the four scanning ranges of $[0, 180^\circ]$, $[0, 150^\circ]$, $[0, 120^\circ]$ and $[0, 90^\circ]$. In this paper, the reconstructed images were processed slice by slice rather than the 3D volumetric images as a whole since it was found that all the DL-based methods can reconstruct high-quality images based on the 2D images. Specifically, We utilize the patch-based strategy for training. The size of the mini-batch is 16. Each patch is 128×128 extracted from the 3D CT volumes slice by slice, and the stride step is 64×64 . In the testing stage, the 2D image with the size of 512×512 is input into the DEDN directly to get high-quality results.

Table I lists the average statistical quantitative evaluation of volumetric images reconstructed by different methods from the four scanning ranges of $[0, 180^\circ]$, $[0, 150^\circ]$, $[0, 120^\circ]$ and $[0, 90^\circ]$, which gives the means and standard deviations (SDs) of RMSE, PSNR and SSIM. From Table I, it can be seen that FDK algorithm has the lowest scores in terms of PSNR and SSIM but the highest RMSE scores when the scanning angle is insufficient, which indicates that the FDK algorithm is sensitive to the completeness of projection data. By minimizing the gradient magnitudes in solving the TV regularized function, the TV algorithm gets better scores compared to FDK. It is observed that all the DL-based methods obtain at least 9.14 HU decrement, 4.5 dB and 0.02 improvements over traditional algorithms regarding RMSE, PSNR and SSIM, which means that DL-based methods could provide more accurate reconstruction results. Although MSWDNet and DCAR are designed for limited-angle CT imaging, they may be worse than DDNet in some cases, which implies that existing reconstruction methods are not always effective for all imaging conditions. Notably, our proposed method achieves the best metrics in all cases. Specifically, SPECIAL brings 3.7 HU and 3.5 HU decrements in RMSE with angular degrees 90° and 120° , 1.89 dB and 1.23 dB promotions in PSNR with angular degrees 180° and 150° , and 0.02 improvement in SSIM with scanning angle 90° compared with other DL-based methods.

As to the AAPM dataset, experiments were performed with four different scanning ranges $[0, 180^\circ]$, $[0, 150^\circ]$, $[0, 120^\circ]$ and $[0, 90^\circ]$ (More results reconstructed with scanning ranges $[0, 180^\circ]$ and $[0, 90^\circ]$ can be found in the supplementary material). Fig. 2 depicts the reconstruction images and the corresponding regions-of-interest (ROIs) of FDK, TV, DDNet, MSWDNet, DCAR and SPECIAL methods with scanning angular angle 150° . From Fig. 2(b1)-(b4), we can see that the FDK algorithm causes serious shadow and streak artifacts across the whole images, which results in the missing and blurring of human tissue features. These confirm the limitation of analytical algorithms in limited-angle CT. It can also be seen in Fig. 2(c1)-(c4) that TV reconstruction fails in artifact suppression and tissue preservation. By exploiting plentiful essential features via deep layer convolutions, DL-based methods exhibit superior performance over traditional approaches. As can be observed in Fig. 2(d1)-(e4), DDNet and MSWDNet methods can greatly

TABLE I

QUANTITATIVE EVALUATIONS (MEANS \pm SDs) OF DIFFERENT METHODS RECONSTRUCTED FROM 180°, 150°, 120° AND 90° FOR THE AAPM DATASET

Range	Metric	FDK	TV	DDNet	MSWDNet	DCAR	SPECIAL
[0, 180°]	RMSE	99.76 \pm 13.00	26.56 \pm 11.75	17.42 \pm 4.34	17.11 \pm 3.88	15.25 \pm 3.36	12.25\pm2.37
	PSNR	28.22 \pm 1.14	40.00 \pm 2.18	43.47 \pm 1.54	43.62 \pm 1.54	44.60 \pm 1.47	46.49\pm1.44
	SSIM	0.7743 \pm 0.0114	0.9638 \pm 0.0090	0.9756 \pm 0.0048	0.9718 \pm 0.0052	0.9809 \pm 0.0048	0.9865\pm0.0034
[0, 150°]	RMSE	135.35 \pm 9.78	43.65 \pm 7.15	25.73 \pm 4.77	28.65 \pm 6.27	27.04 \pm 5.78	22.33\pm4.75
	PSNR	25.67 \pm 0.86	35.50 \pm 1.41	40.09 \pm 1.50	39.21 \pm 1.71	39.68 \pm 1.63	41.32\pm1.65
	SSIM	0.7264 \pm 0.0189	0.9447 \pm 0.0091	0.9690 \pm 0.0060	0.9608 \pm 0.0088	0.9661 \pm 0.0082	0.9769\pm0.0044
[0, 120°]	RMSE	223.58 \pm 14.14	75.50 \pm 15.35	44.10 \pm 9.11	46.57 \pm 9.62	45.67 \pm 8.64	40.59\pm8.28
	PSNR	21.21 \pm 0.88	30.64 \pm 1.72	35.31 \pm 1.74	34.95 \pm 1.71	35.09 \pm 1.64	36.03\pm1.79
	SSIM	0.6315 \pm 0.0238	0.9014 \pm 0.0189	0.9436 \pm 0.0089	0.9261 \pm 0.0136	0.9434 \pm 0.0114	0.9536\pm0.0079
[0, 90°]	RMSE	375.62 \pm 15.19	133.85 \pm 18.27	84.04 \pm 11.91	82.62 \pm 12.58	82.71 \pm 13.80	78.88\pm12.40
	PSNR	16.65 \pm 0.71	25.67 \pm 1.27	29.72 \pm 1.35	29.89 \pm 1.44	29.90 \pm 1.54	30.30\pm1.47
	SSIM	0.5409 \pm 0.0251	0.8017 \pm 0.0225	0.8941 \pm 0.0162	0.8925 \pm 0.0161	0.8909 \pm 0.0161	0.9155\pm0.0126

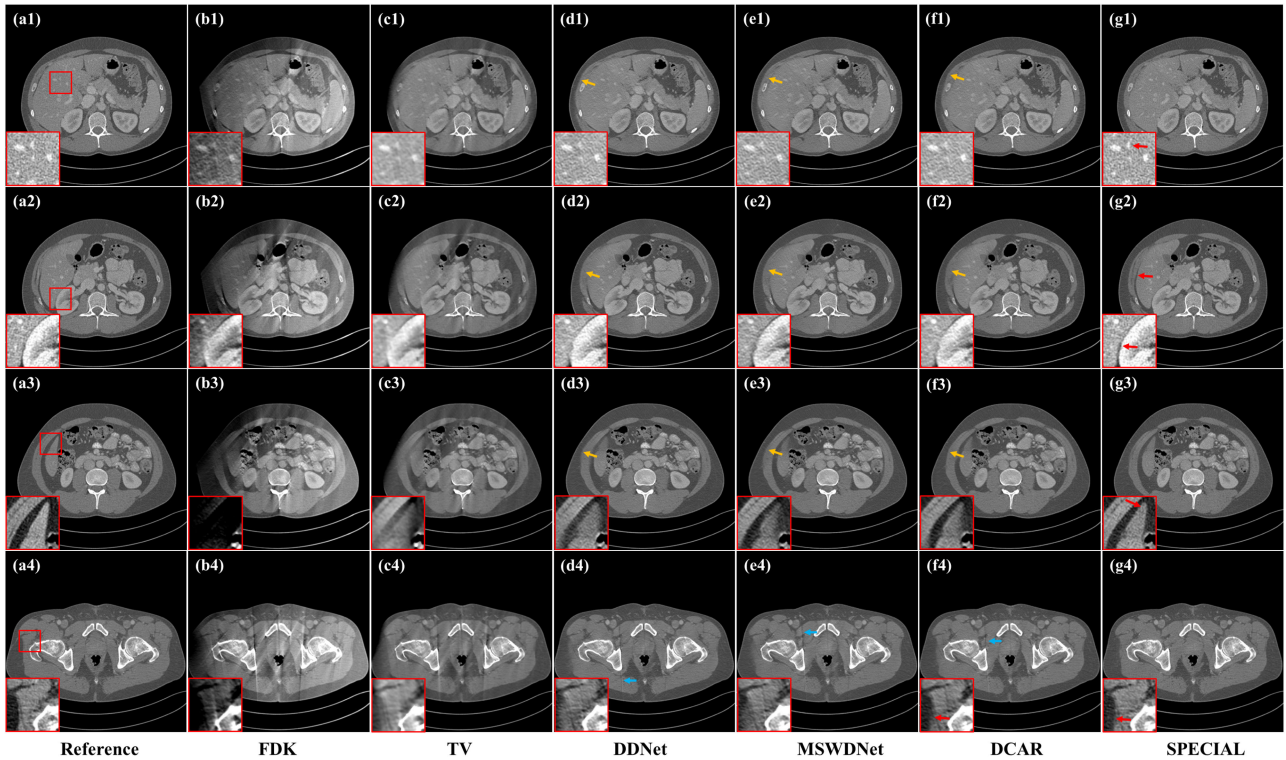


Fig. 2. Reconstruction results from the AAPM dataset for different methods with 150° scanning angular angle. (a1)–(a4) Reference images reconstructed by FDK algorithm from full-sampled projections, (b1)–(b4) images reconstructed by FDK algorithm, (c1)–(c4) images reconstructed by TV method, (d1)–(d4) images processed by DDNet method, (e1)–(e4) images processed by MSWDNet method, (f1)–(f4) images processed by DCAR method, (g1)–(g4) images processed by SPECIAL method. The display window of reconstructed results is [−400, 600] HU, and the display window of ROIs is [−140, 260] HU for a better observation of small details.

improve the reconstruction because it works well in removing artifacts and restoring edges (as pointed by yellow arrows). Nevertheless, residual streak artifacts and tissue blurring can still be well observed (as pointed by the blue arrow and zoomed ROIs in Figs. 2(d4), (e4)). Further, DCAR could improve edge preservation compared to DDNet and MSWDNet (as pointed by the red arrow in Fig. 2(f4)) since it is an iterative-based method and benefits from data consistency term. It is found that the proposed SPECIAL framework can significantly boost the quality of reconstructed images compared to other methods. The proposed method is able to preserve more tissue details

(as pointed by the red arrow in Fig. 2(g1)), reconstruct more clear boundaries between different organs (as indicated by the red arrow in Fig. 2(g2)) and restore sharper edges (as seen in Fig. 2(g3)–(g4)).

Similar observation can be noted for the case with the scanning angular range 120°. From the illustration of Fig. 3(b1)–(b4), we can see that the FDK algorithm only produces seriously degraded CT images, in which the normal organs and tissues are hard to be recognized. Also, such degradation cannot be effectively overcome by the TV method. From the yellow arrows in Fig. 3(d1)–(f4), we can find that DL-based methods work well

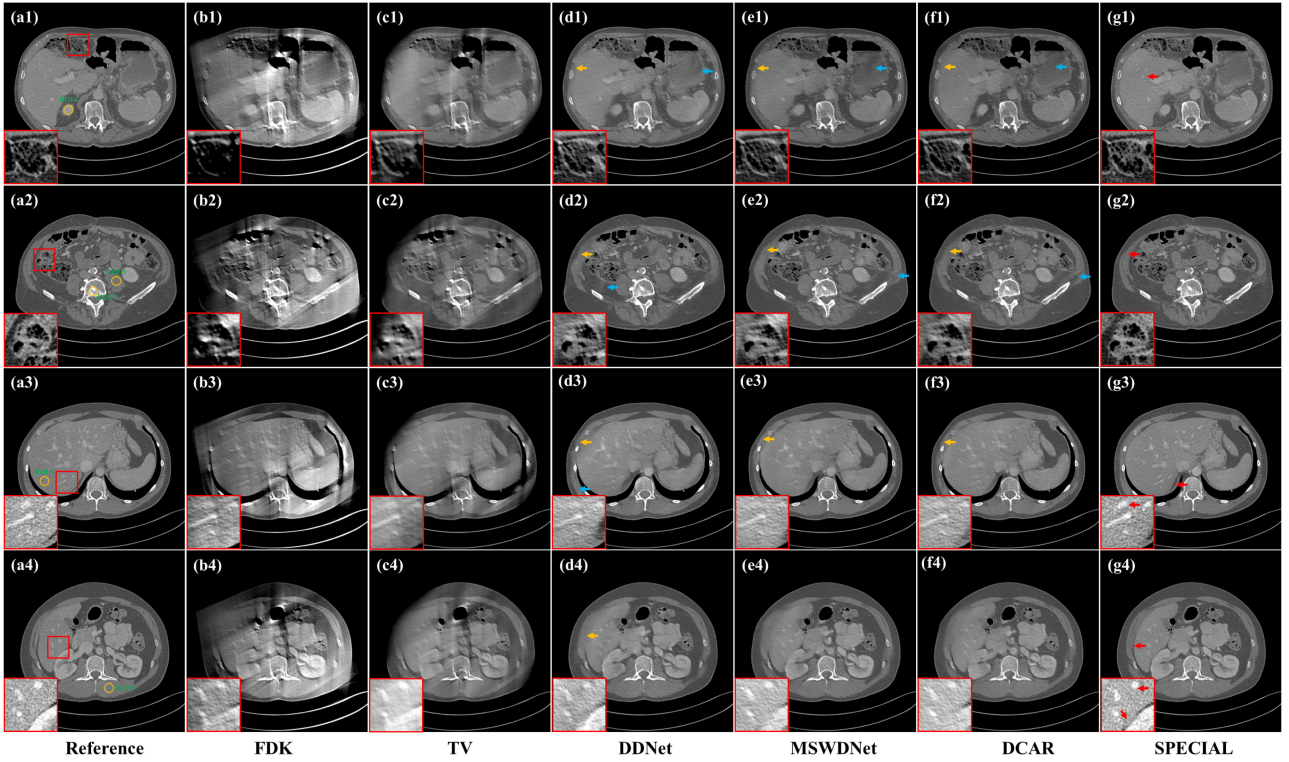


Fig. 3. Reconstruction results from the AAPM dataset for different methods with 120° scanning angular angle, including reconstructed images and magnified ROIs. (a1)–(a4) Reference images reconstructed by FDK algorithm from full-sampled projections, (b1)–(b4) images reconstructed by FDK algorithm, (c1)–(c4) images reconstructed by TV method, (d1)–(d4) images processed by DDNet method, (e1)–(e4) images processed by MSWDNet method, (f1)–(f4) images processed by DCAR method, (g1)–(g4) images processed by SPECIAL method. The display window of reconstructed results is [−400, 600] HU, and the display window of ROIs is [−140, 260] HU for a better observation of small details.

TABLE II
STATISTICAL PROPERTIES (MEANS \pm SDS) OF FIVE FLAT REGIONS RANDOMLY SELECTED FROM FIG. 3 FOR DIFFERENT APPROACHES (UNIT: HU)

	ROI 1	ROI 2	ROI 3	ROI 4	ROI 5
Reference	204 \pm 26	329 \pm 53	-109 \pm 21	116 \pm 25	65 \pm 26
FDK	80 \pm 45	378 \pm 61	-133 \pm 26	193 \pm 23	179 \pm 19
TV	-70 \pm 12	266 \pm 58	-83 \pm 9	145 \pm 12	36 \pm 12
DDNet	122 \pm 20	291 \pm 52	-99 \pm 16	112 \pm 24	66 \pm 19
MSWDNet	152 \pm 19	208 \pm 49	-111 \pm 17	114 \pm 21	66 \pm 20
DCAR	185 \pm 22	269 \pm 50	-96 \pm 16	115 \pm 22	67 \pm 21
SPECIAL	197 \pm 24	297 \pm 57	-103 \pm 21	115 \pm 25	66 \pm 22

in suppressing most artifacts unless some locations pointed by blue arrows. The reconstructed results illustrated in Figs. (2)–(3) indicate that the performances of deep learning type methods are more stable because these data-driven methods learn essential features invariance for CT images. It is also found that the performance of other DL-based methods significantly decreases when the scanning angle is lowered from 150° to 120°, even for DCAR. Experimental results show that the proposed SPECIAL method is quite robust to such projection reduction and can still provide high-quality reconstruction results in terms of artifact reduction, subtle detail restoration (as pointed by red arrows in Fig. 3(g1)–(g4)).

Fig. 4 shows the selected coronal and sagittal views from the reconstructed CT volumes of the AAPM dataset to further

evaluate the visual performance of different DL-based reconstruction methods. It can be observed that all the techniques could successfully suppress most of the artifacts and restore the vast majority of tissue features in all cases. However, from Fig. 4(b1)–(d1), we can see that there are still some artifacts as pointed by the blue arrows. Compared to competitive reconstruction algorithms, the proposed method has the best performance in artifact removal and tissue preservation (as indicated by red arrows in Fig. 4(e1)–(e2)). Again, when the scanning angular angle reduced to 120°, the compared methods will produce more blurring edges of organs and more streak artifacts (as demonstrated by blue arrows in Fig. (b4)–(d4)). Nevertheless, our SPECIAL framework can also lead to clearer boundaries of kidneys and richer subtle vessel details (shown with red arrows in Fig. 4(e3)).

Fig. 5 plots the intensity profiles of sobel maps across the inner structures of CT images provided by different methods reconstructed from 150° and 120°. The profiles show that our SPECIAL framework can produce the closest results to the reference among all competing methods, especially for the edge regions (as pointed by the yellow arrows in Fig. 4).

The mean CT numbers (HU) and SDs of five smooth regions randomly selected from Fig. 3 (as indicated by yellow circles in Fig. 3(a1)–(a4)) are calculated for statistical analysis. And each ROI covers an area of 421 pixels. In Table II, we use the reference images (reconstructed from full-sampled projection data via

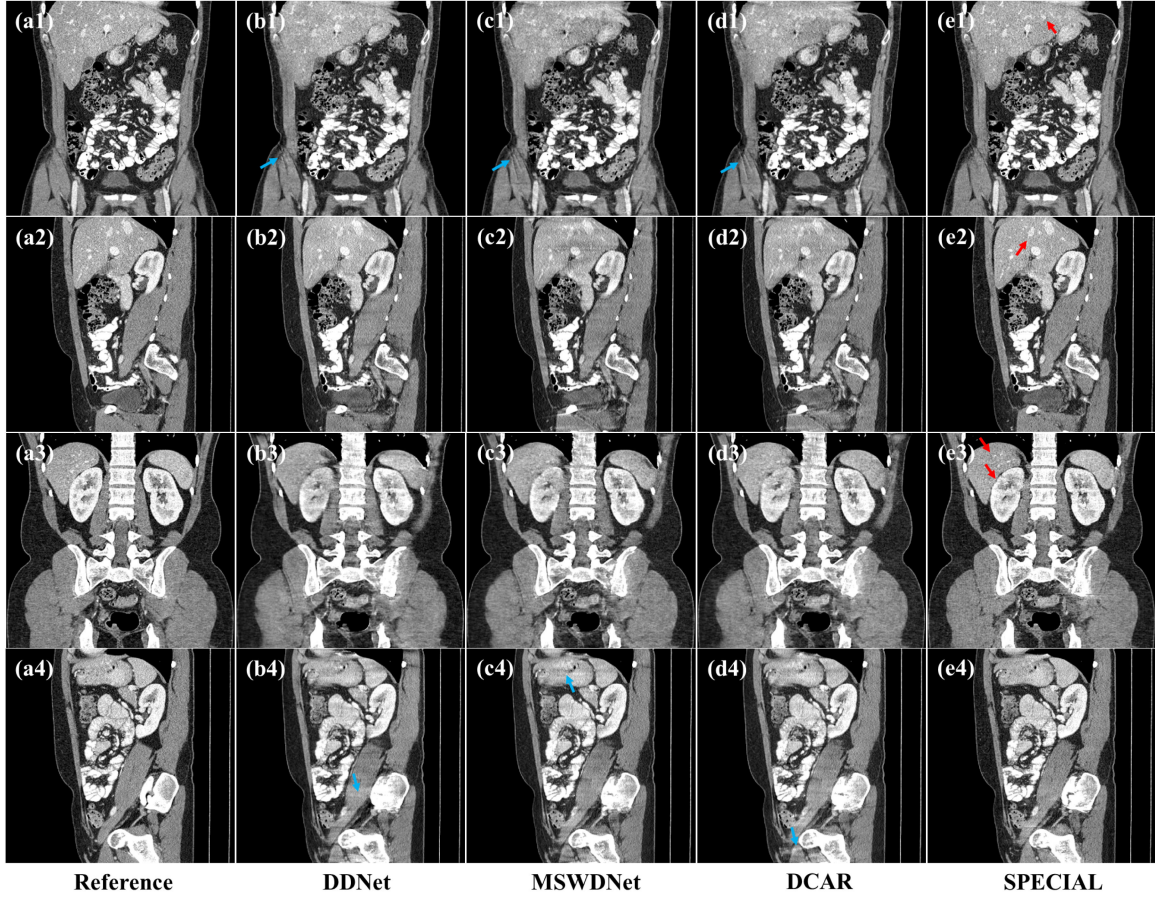


Fig. 4. Coronal and sagittal views from the AAPM dataset for different methods with 150° and 120° scanning angular angles, respectively. (a1)–(e1) Coronal views for different reconstruction methods with 150° scanning angular angle, (a2)–(e2) sagittal views for different reconstruction methods with 150° scanning angular angle, (a3)–(e3) coronal views for different reconstruction methods with 120° scanning angular angle, (a4)–(e4) sagittal views for different reconstruction methods with 120° scanning angular angle. The display window of reconstructed results is [−140, 260] HU.

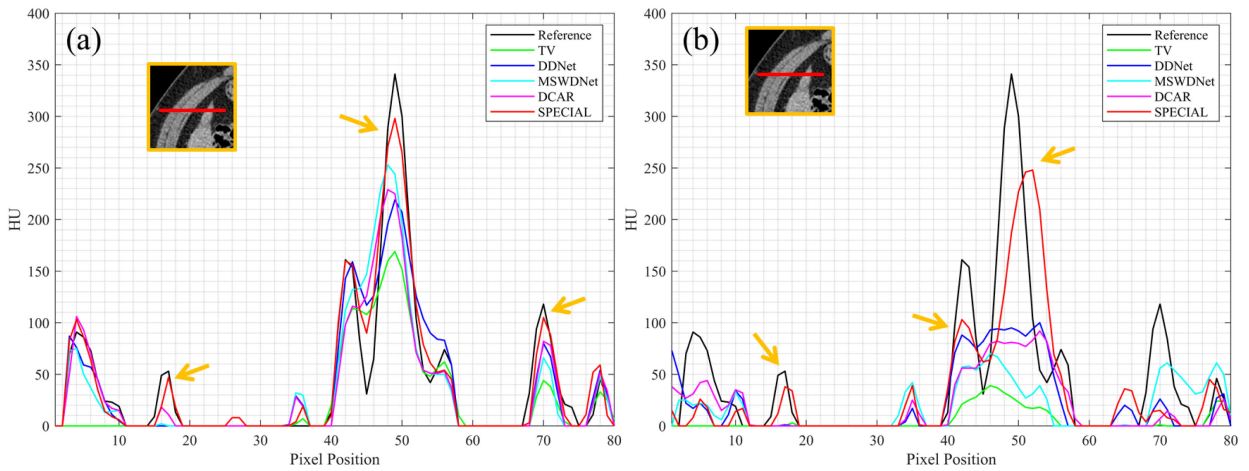


Fig. 5. The intensity profiles of sobel maps along the specified red line in the CT images reconstructed at different scanning angular ranges. (a) Profiles of sobel maps of images reconstructed by various methods from 150°, (b) profiles of sobel maps of images reconstructed by various methods from 120°, respectively.

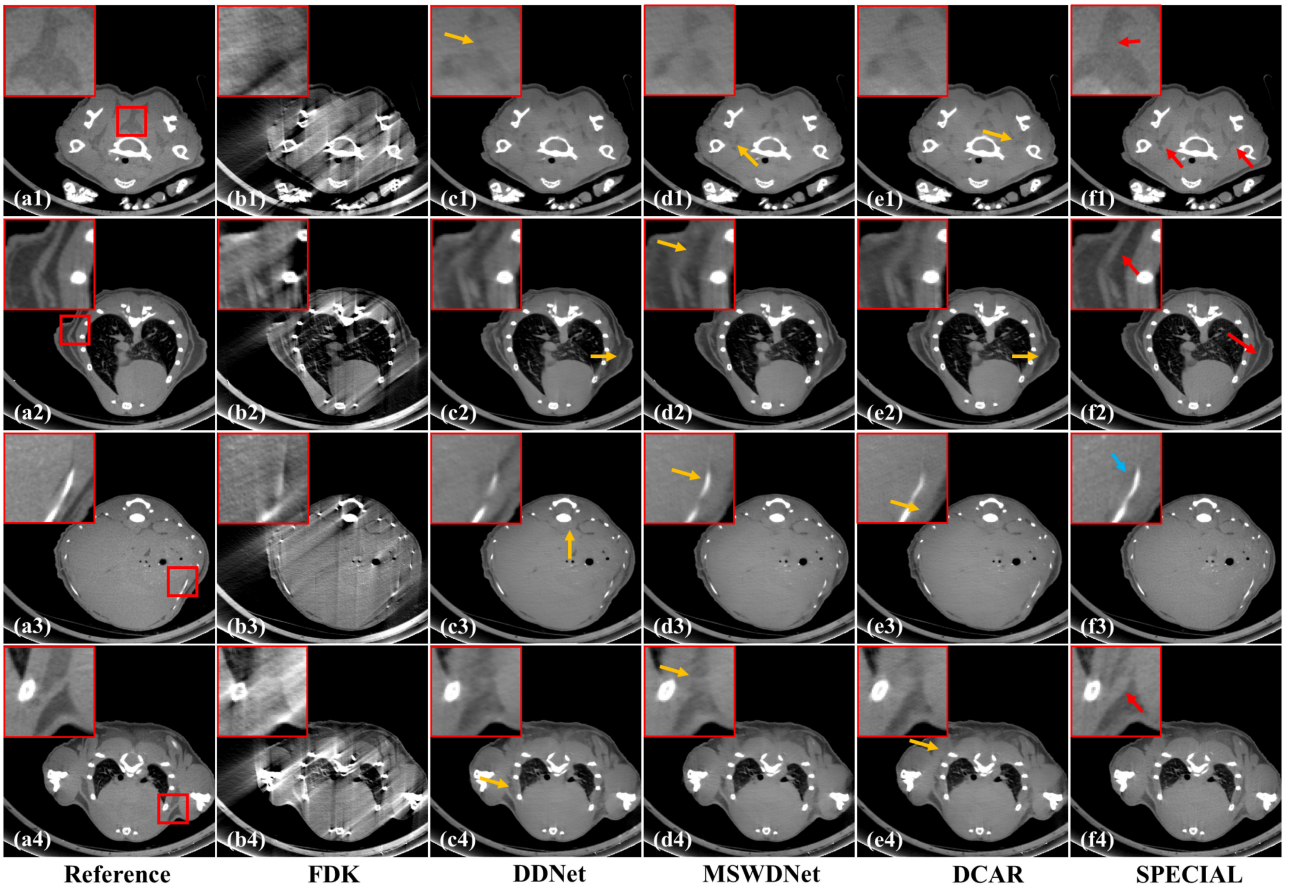


Fig. 6. Reconstruction results from real mice images for different methods with 120° scanning angular angle. (a1)–(a4) Reference images reconstructed by FDK algorithm from full-sampled projections, (b1)–(b4) images reconstructed by FDK algorithm, (c1)–(c4) images processed by DDNet method, (d1)–(d4) images processed by MSWDNet method, (e1)–(e4) images processed by DCAR method, (f1)–(f4) images processed by SPECIAL method. The display window is [−600, 600] HU.

FDK algorithm) as the gold standard to evaluate the statistical properties of different approaches. The FDK algorithm performs unstably, leading to higher mean values and SDs in some regions and lower mean values and SDs in the other regions. This is consistent with the visual observation of the non-uniform artifact distribution in FDK images. Moreover,

TV produces smaller SDs compared to the reference images due to its smoothing effect in reconstruction. The results in Table II show that the DL-based methods have the best overall performance on statistical metrics compared to other methods. Meanwhile, SPECIAL reconstructions have larger SDs than other DL-based methods because the proposed method can generate CT images with high contrast, but other algorithms tend to smooth the reconstructed results (as shown in Figs. 2–3).

B. Real Data Results

Real data experiments were performed to further inspect the performance of the SPECIAL framework in limited-angle CT. The geometry parameters were configured as follows. The tube and detector are Hamamatsu L9421-02 and Dexela1512, respectively. Specifically, the tube voltage and current were 60 kVp and 130 μ A, respectively. The detector had 944 \times 768

units, and each covered an area of 0.072 \times 0.072 mm². The distances from the source to rotation centre and detector were 22 cm and 44 cm, respectively. For one cycle, 1000 projections were collected with cone-beam geometry as the full-sampled projection data. The reconstructed volumetric images had the size of 872 \times 872 \times 600, and each pixel presented the area of 0.072 \times 0.072 \times 0.072 mm³. The reconstructed volumes were sampled from three mice. We selected two of them (600 \times 2 = 1200 images) for training and the third one (600 images) for testing. Again, the 2D patch-based training strategy was employed in real data. The training samples are extracted from the reconstructed volumetric images slice by slice. Each patch has the size of 128 \times 128 with the stride step 64 \times 64. The testing image has the size of 872 \times 872. The reconstructed images of different techniques are illustrated in Fig. 5 with 120° angular range. For better visual observation, all the images in Fig. 5 are cropped to the size of 448 \times 448.

From Fig. 6(b1)–(b4), we can see that the FDK algorithm inevitably leads to severe artifacts wherein tissues, organs and bones are degraded seriously when the scanning range is less than 180°. The DDNet and MSWDNet methods can be used to remove the artifacts and preserve edges as illustrated in Fig. 6(c1)–(d4). Nevertheless, they also produce fake textures

TABLE III
COMPUTATIONAL COST OF DIFFERENT METHODS (UNIT: SECOND)

Method	TV	DDNet	MSWDNet	DCAR	SPECIAL
Time	7940.0	7.5	8.7	150.6	24.6

TABLE IV
QUANTITATIVE EVALUATIONS OF DIFFERENT STAGES OF SPECIAL FOR AAPM IMAGES RECONSTRUCTED FROM 180°, 150°, 120° AND 90°

Range	Metric	Out_{S1}	Out_{S2}	Out_{S3}
[0, 180°]	RMSE	16.24	13.09	12.25
	PSNR	44.06	45.93	46.49
	SSIM	0.9797	0.9842	0.9865
[0, 150°]	RMSE	26.39	23.72	22.33
	PSNR	39.87	40.80	41.32
	SSIM	0.9660	0.9722	0.9769
[0, 120°]	RMSE	44.71	43.24	40.59
	PSNR	35.19	35.48	36.03
	SSIM	0.9380	0.9426	0.9536
[0, 90°]	RMSE	84.19	83.48	78.88
	PSNR	29.73	29.81	30.30
	SSIM	0.8740	0.8850	0.9155

and blurs tiny details (as pointed by yellow arrows in Fig. 6(c1)–(d4)). Again, it can be noticed from Fig. 6(e1)–(e4) that DCAR still inevitably fails to reconstruct high-quality images when the scanning angular range is small. With the help of high-frequency constraint and measurement consistency in the algorithm framework, the SPECIAL method brings further improved reconstruction performance. From the locations pointed by red arrows in Fig. 6(f1)–(f4), we can conclude that the proposed method also achieve the best performance in restoring and preserving organ or tissue features. It is also noted that even restricted by the scale of training samples, the proposed SPECIAL framework also suffers from detail blurring (as pointed by the blue arrow in Fig. 6(f3)). More coronal and sagittal results can be found in section C. *Real Data Results* in the supplementary material.

C. Computational Cost

Table III lists the computational cost of different methods with processing 200 CT images reconstructed with 120° scanning angular angle from AAPM Challenge Data. TV spends the longest time because of the complex iterative process, and it still fails to reconstruct high-quality images. Both DDNet and MSWDNet are image domain-based methods that take much less time and achieve better performance than traditional reconstruction algorithms. DCAR and SPECIAL are iterative-based methods and converge faster than conventional IR algorithms due to the assistance of DL-based methods. Specifically, the proposed method can obtain the best performance within the appropriate time.

D. Analysis for PI Strategy

Table IV is used to quantitatively evaluate the contributions of different phases in the SPECIAL framework. In terms of RMSE, PSNR and SSIM scores, the progressive improvements of different modules can be well observed in Table IV. Specifically, Out_{S2} obtains lower RMSE, higher PSNR and SSIM than Out_{S1} .

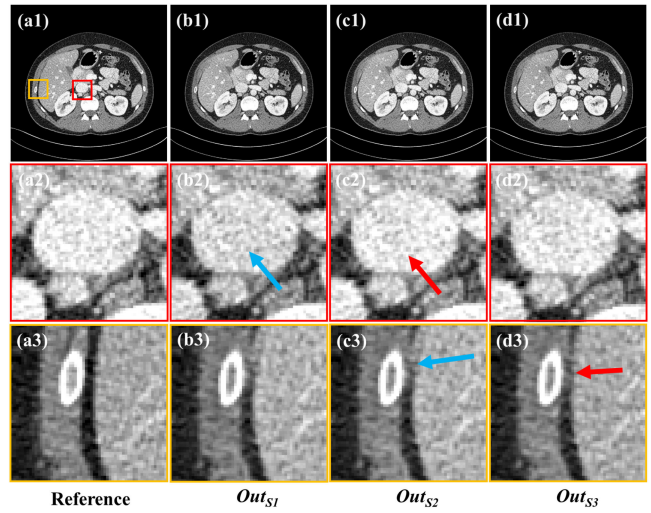


Fig. 7. Reconstruction results from the AAPM dataset for different stages of SPECIAL with 150° scanning angular angle. (a1)–(a3) Reference images reconstructed by FDK algorithm from full-sampled projections, (b1)–(b3) images processed by the first stage of SPECIAL, (c1)–(c3) images processed by the second stage of SPECIAL, (d1)–(d3) images processed by the third stage of SPECIAL, (e1)–(e4) images processed by SPECIAL method. The display window is [−140, 260] HU.

because of the correction module. That means Out_{S2} is closer to the reference image in terms of CT values and image textures. After this, EGAN is conducted again to refine Out_{S2} , leading to Out_{S3} with further higher metric values.

Moreover, to further evaluate the mechanism of PI strategy, the outputted CT images from different stages of the proposed method with scanning range 150° are accessed. We can see that Out_{S1} successfully removes artifacts and restores the high-frequency component as shown in Fig. 7(b1). However, Out_{S1} leads to lowered CT numbers with respect to the reference (as pointed by the blue arrow in Fig. 7(b2)). The reason might be the non-uniformly distributed artifacts caused by projection missing. With the correction operator applied in Out_{S2} , from the tissue pointed by the red arrow in Fig. 7(c2), we can observe that the CT numbers are higher compared to Out_{S1} and the corresponding ROI is visually closer to the reference image. Moreover, the correction operator in the SPECIAL framework requires much less computational cost than the IR methods under the precondition of measurement consistency since it only involves a single projection operation and FDK reconstruction rather than iterative processing. Out_{S3} further promotes the performance of Out_{S2} (comparing the results in Fig. 7(c3) and Fig. 7(d3)) by using another EGAN to refine the results provided by the previous stage. Both qualitative and quantitative results validate the effectiveness of the PI strategy used in the SPECIAL framework.

E. Ablation Study

In this section, we perform an ablation study to investigate the effectiveness of the high-frequency enhanced module utilized in EGAN (see more details in Fig. 1(b)). DEDN and WGAN are

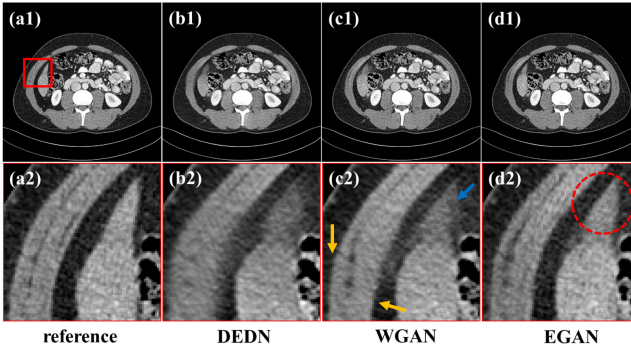


Fig. 8. Reconstruction results from the AAPM dataset for different modules with 150° scanning angular angle. (a1) Reference image reconstructed by FDK algorithm from full-sampled projections, (b1) image processed by DEDN, (c1) images processed by WGAN, (d1) image processed by EGAN. (a2)–(d2) are the magnified ROIs. The display window is $[-140, 260]$ HU.

treated as comparisons. Specifically, WGAN is as same as the EGAN except for the high-frequency enhancement module.

Reconstructions of different modules from 150° are depicted in Fig. 8. From Fig. 8(b1), we can see that DEDN performs well in artifact removal and tissue restoration. However, its reconstructions still suffer from over-smoothing and fake structures shown in Fig. 8(b2). Compared to DEDN, WGAN could provide better visual perception and clearer boundaries (as pointed by the yellow arrows in Fig. 8(c2)), which verifies the contrast improvement brought by the adversarial learning strategy. However, from the blue arrow in Fig. 8(c2), we can observe that the WGAN still suffers from edge blurs. Aided by the high-frequency enhancement module, the EGAN module could generate clearer boundaries between tissues (as presented by the red circle in Fig. 8(d2)) by the processing upon high-frequency components.

IV. CONCLUSION

Existing direct image-domain-based reconstruction algorithms [16], [36], [37], [44], [51] cannot guarantee the reconstructed image is consistent with the measurement since there is no feedback mechanism like the IR schemes [30]. Meanwhile, they seldom utilize additional prior knowledge to improve the reconstruction. Besides, those DL-based methods embedded in iterative optimization usually have difficulty in hyper-parameter selection. Therefore, to address these problems, our SPECIAL framework incorporates projection correction into enhanced adversarial learning and adopts a PI strategy to improve the reconstructed results gradually. In the first stage, EGAN module is employed upon high-frequency component to alleviate contrast losing caused by over-smoothing. Then, to ensure the worst performance, we provide a lightweight operator in sinogram space to ensure the measurement consistency. After this, EGAN is used again to refine images provided by the previous stage. Experimental results based on simulated and real data reconstructed from different scanning ranges are performed to validate the effectiveness of the proposed method. Compared to other algorithms, the SPECIAL framework performs better in artifact suppression, tissue recovery and edge preservation.

Although the SPECIAL framework demonstrates encouraging improvement in limited-angle CT reconstruction, there are still some issues to be noticed. First, EGAN can also negatively influence the reconstructed images because the high-frequency extractor used in this paper might not be the most optimal solution. Therefore, how to design a more effective constraint on the high-frequency component is still an opening issue. Second, the correction operator is modified from FDK, which inevitably brings some secondary artifacts that degrade the reconstruction images. So better approaches to ensure the measurement consistency are still needed to be explored in further work. Third, SPECIAL is an iterative-based method with a combination of deep learning and iterative optimization. It is still a challenge to incorporate deep learning into a conventional iterative strategy effectively. Last, the noise will be enhanced when employing the high-frequency extraction since the noise represents high-frequency signals. It is significant to avoid the amplification of noise while extracting high-frequency components.

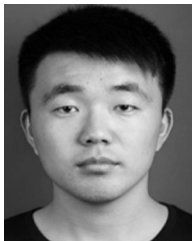
ACKNOWLEDGMENT

The authors are grateful to thank Dr. Cynthia McCollough (the Mayo Clinic, USA) for providing clinical projection data of Somatom Definition AS+ CT. The authors are also grateful to the anonymous reviewers for their valuable comments.

REFERENCES

- [1] G. Wang, H. Y. Yu, and B. De Man, "An outlook on X-ray CT research and development," *Med. Phys.*, vol. 35, no. 3, pp. 1051–1064, Mar. 2008.
- [2] M. K. Cho *et al.*, "A feasibility study of digital tomosynthesis for volumetric dental imaging," *J. Instrum.*, vol. 7, Mar., 2012, Art. no. P03007.
- [3] A. Tingberg, "X-ray tomosynthesis: A review of its use for breast and chest imaging," *Radiat. Protect. Dosimetry*, vol. 139, no. 1-3, pp. 100–107, 2010.
- [4] C. Gong and L. Zeng, "Self-guided limited-angle computed tomography reconstruction based on anisotropic relative total variation," *IEEE Access*, vol. 8, pp. 70465–70476, 2020.
- [5] W. Wu, D. Hu, K. An, S. Wang, and F. Luo, "A high-quality photon-counting CT technique based on weight adaptive total-variation and image-spectral tensor factorization for small animals imaging," *IEEE Trans. Instrum. Meas.*, vol. 70, Sept. 2021, Art. no. 2502114.
- [6] Z. Q. Chen *et al.*, "A limited-angle CT reconstruction method based on anisotropic TV minimization," *Phys. Med. Biol.*, vol. 58, no. 7, pp. 2119–2141, Apr. 2013.
- [7] C. X. Wang and L. Zeng, "Error bounds and stability in the ℓ_0 regularized for CT reconstruction from small projections," *Inverse Problem Imag.*, vol. 10, no. 3, pp. 829–853, Aug. 2016.
- [8] M. Xu, D. Hu, F. Luo, F. Liu, S. Wang, and W. Wu, "Limited angle x ray CT reconstruction using image gradient ℓ_0 norm with dictionary learning," *IEEE Trans. Radiat. Plasma Med. Sci.*, vol. 5, no. 1, pp. 78–87, Jan. 2021.
- [9] W. W. Wu *et al.*, "Low-dose spectral CT reconstruction using image gradient $\ell(0)$ -norm and tensor dictionary," *Appl. Math. Model.*, vol. 63, pp. 538–557, Nov. 2018.
- [10] W. Yu, C. X. Wang, and M. Huang, "Edge-preserving reconstruction from sparse projections of limited-angle computed tomography using ℓ_0 -regularized gradient prior," *Rev. Sci. Instrum.*, vol. 88, no. 4, Apr. 2017, Art. no. 10.
- [11] Y. L. Sun and J. X. Tao, "Image reconstruction from few views by ℓ_0 -norm optimization," *Chin. Phys. B*, vol. 23, no. 7, Jul. 2014, Art. no. 5.
- [12] W. Wu, F. Liu, Y. Zhang, Q. Wang, and H. Yu, "Non-local low-rank cube-based tensor factorization for spectral CT reconstruction," *IEEE Trans. Med. Imag.*, vol. 38, no. 4, pp. 1079–1093, Apr. 2019.
- [13] X. Luo, W. Yu, and C. Wang, "An image reconstruction method based on total variation and wavelet tight frame for limited-angle cT," *IEEE Access*, vol. 6, pp. 1461–1470, 2018.

- [14] D. Hu *et al.*, "SISTER: Spectral-image similarity-based tensor with enhanced-sparsity reconstruction for sparse-view multi-energy cT," *IEEE Trans. Comput. Imag.*, vol. 6, pp. 477–490, Nov. 2020.
- [15] Y. Huang *et al.*, "Scale-space anisotropic total variation for limited angle tomography," *IEEE Trans. Radiat. Plasma Med. Sci.*, vol. 2, no. 4, pp. 307–314, Jul. 2018.
- [16] E. Kang, W. Chang, J. Yoo, and J. C. Ye, "Deep convolutional framelet denoising for low-dose CT via wavelet residual network," *IEEE Trans. Med. Imag.*, vol. 37, no. 6, pp. 1358–1369, Jun. 2018.
- [17] E. Kang, J. Min, and J. C. Ye, "A deep convolutional neural network using directional wavelets for low-dose X-ray CT reconstruction," *Med. Phys.*, vol. 44, no. 10, pp. e360–e375, Oct. 2017.
- [18] J. M. Wolterink, T. Leiner, M. A. Viergever, and I. Işgum, "Generative adversarial networks for noise reduction in low-dose cT," *IEEE Trans. Med. Imag.*, vol. 36, no. 12, pp. 2536–2545, Dec. 2017.
- [19] Y. Zhang *et al.*, "CD-Net: Comprehensive domain network with spectral complementary for DECT sparse-view reconstruction," *IEEE Trans. Comput. Imag.*, vol. 7, pp. 436–447, Apr. 2021.
- [20] W. Wu, D. Hu, C. Niu, H. Yu, V. Vardhanabhuti, and G. Wang, "DRONE: Dual-domain residual-based optimization network for sparse-view CT reconstruction," *IEEE Trans. Med. Imag.*, to be published, doi: [10.1109/TMI.2021.3078067](https://doi.org/10.1109/TMI.2021.3078067).
- [21] D. Hu *et al.*, "hybrid domain neural network processing for sparse-view CT reconstruction," *IEEE Trans. Radiat. Plasma Med. Sci.*, vol. 5, no. 1, pp. 88–98, Jan. 2021.
- [22] X. Yin *et al.*, "Domain progressive 3D residual convolution network to improve low dose CT imaging," *IEEE Trans. Med. Imag.*, vol. 38, no. 12, pp. 2903–2913, Dec. 2019.
- [23] Q. Zhang *et al.*, "Artifact removal using a hybrid-domain convolutional neural network for limited-angle computed tomography imaging," *Phys. Med. Biol.*, vol. 65, no. 15, 2020, Art. no. 155010.
- [24] T. Würfl *et al.*, "Deep learning computed tomography: Learning projection-domain weights from image domain in limited angle problems," *IEEE Trans. Med. Imag.*, vol. 37, no. 6, pp. 1454–1463, Jun. 2018.
- [25] Y. Dong *et al.*, "FD-GAN: Generative adversarial netw. with fusion-discriminator for single image dehazing," in *Proc. AAAI*, 2020, pp. 10729–10736.
- [26] I. Goodfellow, J. Pouget-Abadie, M. Mirza *et al.*, "Generative adversarial nets," in *Proc. Neural Inf. Process. Syst.*, 2014, pp. 2672–2680.
- [27] I. Gulrajani *et al.*, "Improved training of wasserstein gans," in *Proc. Neural Inf. Process. Syst.*, 2017, pp. 5767–5777.
- [28] R. Anirudh *et al.*, "Lose the views: Limited angle CT reconstruction via implicit sinogram completion," in *Proc. Conf. Comput. Vis. Pattern Recognit.*, 2018, pp. 6343–6352.
- [29] Z. Liu *et al.*, "TomoGAN: Low-dose synchrotron X-ray tomography with generative adversarial networks: Discussion," *J. Opt. Soc. Amer. A*, vol. 37, pp. 422, Mar. Jan., 2020.
- [30] H. Gupta, K. H. Jin, H. Q. Nguyen, M. T. McCann, and M. Unser, "CNN-based projected gradient descent for consistent CT image reconstruction," *IEEE Trans. Med. Imag.*, vol. 37, no. 6, pp. 1440–1453, Jun. 2018.
- [31] T. A. Bubba *et al.*, "Learning the invisible: A hybrid deep learning-shearlet framework for limited angle computed tomography," *Inverse Probl.*, vol. 35, no. 6, 2019, Art. no. 064002.
- [32] J. Wang *et al.*, "ADMM-based deep reconstruction for limited-angle cT," *Phys. Med. Biol.*, vol. 64, no. 11, 2019, Art. no. 115011.
- [33] B. Zhou, S. K. Zhou, J. S. Duncan, and C. Liu, "Limited view tomographic reconstruction using a cascaded residual dense spatial-channel attention network with projection data fidelity layer," *IEEE Trans. Med. Imag.*, vol. 40, no. 7, pp. 1792–1804, Jul. 2021.
- [34] H. Zhang, B. Liu, H. Yu, and B. Dong, "MetaInv-Net: Meta inversion network for sparse view CT image reconstruction," *IEEE Trans. Med. Imag.*, vol. 40, no. 2, pp. 621–634, Feb. 2021.
- [35] B. Zhu *et al.*, "Image reconstruction by domain-transform manifold learning," *Nature*, vol. 555, no. 7697, pp. 487–492, 2018.
- [36] K. H. Jin, M. T. McCann, E. Froustey, and M. Unser, "Deep convolutional neural network for inverse problems in imaging," *IEEE Trans. Image Process.*, vol. 26, no. 9, pp. 4509–4522, Sep. 2017.
- [37] Y. Han and J. C. Ye, "Framing U-Net via deep convolutional framelets: Application to sparse-view cT," *IEEE Trans. Med. Imag.*, vol. 37, no. 6, pp. 1418–1429, Jun. 2018.
- [38] O. Ronneberger, P. Fischer, and T. Brox, "U-net: Convolutional networks for biomedical image segmentation," in *Proc. MICCAI*, 2015, pp. 234–241.
- [39] K. Zhang, W. Zuo, Y. Chen, D. Meng, and L. Zhang, "Beyond a gaussian denoiser: Residual learning of deep cnn for image denoising," *IEEE Trans. Image Process.*, vol. 26, no. 7, pp. 3142–3155, Jul. 2017.
- [40] K. He *et al.*, "Deep residual learning for image recognition," in *Proc. Conf. Comput. Vis. Pattern Recognit.*, 2016, pp. 770–778.
- [41] R. K. Srivastava, K. Greff, and J. Schmidhuber, "Training very deep networks," in *Proc. Neural Inf. Process. Syst.*, 2015, pp. 2377–2385.
- [42] G. Huang *et al.*, "Densely connected convolutional networks," in *Proc. Conf. Comput. Vis. Pattern Recognit.*, 2017, pp. 2261–2269.
- [43] Y. Zhang *et al.*, "Residual dense network for image super-resolution," in *Proc. Conf. Comput. Vis. Pattern Recognit.*, 2018, pp. 2472–2481.
- [44] Z. C. Zhang, X. K. Liang, X. Dong, Y. Xie, and G. Cao, "A sparse-view CT reconstruction method based on combination of densenet and deconvolution," *IEEE Trans. Med. Imag.*, vol. 37, no. 6, pp. 1407–1417, Jun. 2018.
- [45] S. Ioffe and C. Szegedy, "Batch normalization: Accelerating deep network training by reducing internal covariate shift," in *Proc. Int. Conf. Mach. Learn.*, Jun. 2015, pp. 448–456.
- [46] A. Krizhevsky, I. Sutskever, and G. E. Hinton, "Imagenet classification with deep convolutional neural networks," *Proc. Neural Inf. Process. Syst.*, 2012, pp. 1097–1105.
- [47] Q. Yang *et al.*, "Low-dose CT image denoising using a generative adversarial network with wasserstein distance and perceptual loss," *IEEE Trans. Med. Imag.*, vol. 37, no. 6, pp. 1348–1357, Jun. 2018.
- [48] H. Chen *et al.*, "LEARN: Learned experts' assessment-based reconstruction network for sparse-data cT," *IEEE Trans. Med. Imag.*, vol. 37, no. 6, pp. 1333–1347, Jun. 2018.
- [49] H. Shi *et al.*, "A novel iterative CT reconstruction approach based on FBP algorithm," *PLoS One*, vol. 10, no. 9, 2015, Art. no. e0138498.
- [50] D. Kingma and J. Ba, "Adam: A method for stochastic optimization," in *Proc. Int. Conf. Learn. Representations*, 2014, pp. 1–13.
- [51] J. Gu and J. C. Ye, "Multi-scale wavelet domain residual learning for limited-angle CT reconstruction," in *Proc. Fully Three-Dimensional Image Reconstruction Radiol. Nucl. Med. (Fully3D)*, Jun. 2017, pp. 443–447.
- [52] Y. Huang *et al.*, "Data consistent artifact reduction for limited angle tomography with deep learning prior," in *Proc. Int. Workshop Mach. Learn. Med. Image Reconstruction*, 2019, pp. 101–112.
- [53] W. Zhou, A. C. Bovik, H. R. Sheikh, and E. P. Simoncelli, "Image quality assessment: From error visibility to structural similarity," *IEEE Trans. Image Process.*, vol. 13, no. 4, pp. 600–612, Apr. 2004.
- [54] Y. Li, M. A. Speidel, C. J. Francois, and G.-H. Chen, "Radiation dose reduction in CT myocardial perfusion imaging using SMART-RECON," *IEEE Trans. Med. Imag.*, vol. 36, no. 12, pp. 2557–2568, Dec. 2017.



Dianlin Hu received the B.S. degree from the China University of Mining and Technology, Xuzhou, China, in 2017. He is currently working toward the Ph.D. degree with the Laboratory of Image Science and Technology, School of Computer Science and Engineering, Southeast University, Nanjing, China. His research interests include sparse-view computed tomography reconstruction and spectral image reconstruction.



Yikun Zhang received the B.S. and M.E. degrees from the China University of Mining and Technology, Xuzhou, China, in 2017 and 2019, respectively. He is currently working toward the Ph.D. degree with the Laboratory of Image Science and Technology, School of Computer Science and Engineering, Southeast University, Nanjing, China. His current research interests include medical image reconstruction, material decomposition, and deep learning.



Jin Liu received the Ph.D. degree from Southeast University, Nanjing, China, in 2018. Since 2018, he has been a Faculty Member with the Department of Computer and Information, Anhui Polytechnic University, Wuhu, China. His research interests include low-dose computed tomography reconstruction and medical image processing.



Guotao Quan received the Ph.D. degree from the Huazhong University of Science and Technology, Wuhan, China, in 2011. Since 2011, he has been a Faculty Member with United Imaging, Shanghai, China. His research interests include medical image processing and deep learning-base image processing.



Changping Du received the B.E. degrees from the Cuiying Honors College, Lanzhou University, Lanzhou, China, in 2019. He is currently working toward the Ph.D. degree with the Laboratory of Image Science and Technology, School of Computer Science and Engineering, Southeast University, Nanjing, China. His current research interests include image processing and machine learning.



Qiegen Liu (Senior Member, IEEE) received the B.S. degree in applied mathematics from Gannan Normal University, Ganzhou, China, the M.S. degree in computation mathematics, and the Ph.D. degree in biomedical engineering from Shanghai Jiaotong University, Shanghai, China. Since 2012, he has been with School of Information Engineering, Nanchang University, Nanchang, China, where he is currently a Professor. During 2015–2017, he was also a Postdoc with UIUC and University of Calgary, Calgary, AB, Canada. His current research interests include sparse representations, deep learning, and their applications in image processing, computer vision, and MRI reconstruction.



Jinglin Zhang received the M.S. degree in circuits and systems from Shanghai University, Shanghai, China, in 2010 and the Ph.D. degree in electronics and telecommunications from the National Institute of Applied Sciences-Rennes, Rennes, France, in 2013. He is on the Faculty of the School of Artificial Intelligence, Hebei University of Technology, Tianjin, China. His current research interests include computer vision, high-performance computing, and interdisciplinary research with pattern recognition and atmospheric science.



Yang Chen (Senior Member, IEEE) received the M.S. and Ph.D. degrees in biomedical engineering from Southern Medical University, Guangzhou, China, in 2004 and 2007, respectively. Since 2008, he has been a Faculty Member with the Department of Computer Science and Engineering, Southeast University, Nanjing, China. His research interests include medical image reconstruction, image analysis, pattern recognition, and computerized-aid diagnosis.



Shouhua Luo received the Ph.D. degree from Southeast University, Nanjing, China, in 2004. Since 2005, he has been a Faculty Member with the Department of Biomedical Engineering, Southeast University. His research interests include image processing and cone-beam CT imaging.



Limin Luo (Senior Member, IEEE) received the Ph.D. degree from the University of Rennes 1, Rennes, France, in 1986. He is currently a Professor with the Department of Computer Science and Engineering, Southeast University, Nanjing, China. His research interests include medical imaging, image analysis, computer-assisted systems for diagnosis and therapy in medicine, and computer vision.